Article

Not peer-reviewed version

Hierarchical Super-Hydrophilic Aluminum Oxide Architectures on Textured Silicon for Aqueous and Vapor-Phase Interaction

Hyo-Ryoung Lim †, Tae Woong Yun †, Nu Si A Eom, Doyoun Kim, Chae Yeon Hong, Yong-Ho Choa *

Posted Date: 25 September 2025

doi: 10.20944/preprints202509.1977.v1

Keywords: super-hydrophilicity; hierarchical oxide structures; surface functionalization; adsorption–desorption dynamics; chemosensing interfaces

 doi:10.20944/preprints202509.1977.v1

Article

Hierarchical Super-Hydrophilic Aluminum Oxide Architectures on Textured Silicon for Aqueous and Vapor-Phase Interaction

Hyo-Ryoung Lim [1,†], Tae Woong Yun [2,†], Nu Si A Eom [3], Doyoun Kim [1], Chae Yeon Hong [4] and Yong-Ho Choa [2,*]

[1] Major of Human Bioconvergence, Pukyong National University, Busan 48513, Republic of Korea
[2] Department of Materials Science and Chemical Engineering, Hanyang University, Ansan 15588, Republic of Korea
[3] Display Research Center, Korea Electronics Technology Institute, Seongnam 13509, Republic of Korea
[4] Department of Biotechnology, Pukyong National University, Busan 48513, Republic of Korea
* Correspondence: choa15@hanyang.ac.kr; Tel.: 031-400-5650
† These authors contributed equally to this work.

Abstract

Hierarchical super-hydrophilic surfaces were realized by forming porous anodic aluminum oxide (AAO) and boehmite [AlO(OH)] on micro-textured Si wafers. One-step anodization of e-beam-deposited Al followed by controlled pore-widening, thermal annealing, or hot-water treatment produced oxide architectures exhibiting near-zero water contact angles (aqueous regime) and pronounced H_2O adsorption–desorption responses (vapor regime). Thermogravimetric analysis, moisture isotherms, and FT-IR indicate that increased porosity and anion incorporation (O^-/O^{2-}/oxalate) enrich surface hydroxyl functionality, enhancing affinity to H_2O. The results delineate two complementary regimes—rapid capillary wetting and multilayer vapor adsorption—supporting the use of these oxide/Si hierarchies as interactive water-affine interfaces with potential relevance to moisture gettering and chemosensing.

Keywords: super-hydrophilicity; hierarchical oxide structures; surface functionalization; adsorption–desorption dynamics; chemosensing interfaces

1. Introduction

The miniaturization of micro-electro-mechanical systems (MEMS) has driven significant technological advances across optical, radio-frequency, and sensing applications over the past few decades[1–3]. However, the extreme scale reduction and high surface area-to-volume ratios inherent in MEMS components introduce critical reliability challenges, particularly moisture-induced stiction between silicon (Si) surfaces and moving parts[4–6]. Stiction phenomena arise from multiple physical mechanisms including Van der Waals forces, capillary adhesion, chemical bonding, electrostatic interactions, and residual stress[7]. Among these factors, residual moisture poses the most severe threat, as adsorbed water molecules can form destructive capillary bridges and hydrogen bonds due to the high dielectric dipole moment of H_2O[4–5]. Ensuring reliable hermetically sealed MEMS packages requires maintaining water vapor concentrations below 5,000 ppm, while optimal performance demands internal relative humidity (RH) below 20%[6–8].

The challenge of moisture management in MEMS environments has created substantial demand for both passive moisture gettering systems and active moisture sensing technologies. Traditional moisture getters rely on hydrophilic solid adsorbents that exploit strong hydrogen bonding with water vapor through high heats of adsorption[6,9]. Conventional designs incorporate solid desiccants dispersed in hygroscopic polymer matrices[10–11] or high-surface-area ceramics integrated within

 doi:10.20944/preprints202509.1977.v1

package walls[5,6,12]. Complementing these passive approaches, capacitive moisture sensors based on MEMS technology have emerged as critical components for real-time humidity monitoring in semiconductor packaging, industrial process control, and environmental applications. These sensors typically employ moisture-sensitive dielectric materials positioned between permeable electrodes, exhibiting capacitance changes proportional to ambient humidity levels.

Among metal oxide candidates, aluminum oxide (Al_2O_3) has garnered attention for both moisture gettering and sensing applications due to its exceptional water affinity properties[13–16]. The high polarizing power of Al enables spontaneous H_2O dissociation into surface hydroxyls at room temperature, with unsaturated surface Al sites functioning as strong Lewis acid centers[17–19]. Nanoporous anodic aluminum oxide (AAO) structures have demonstrated particular promise as humidity sensors, offering systematic control over sensitivity through manipulation of pore diameter, pore density, and layer thickness. The unique combination of high surface area, tunable porosity, and intrinsic hydrophilicity makes AAO an attractive candidate for both passive moisture adsorption and active moisture detection.

Surface wettability engineering has emerged as a complementary approach to enhance moisture-responsive behaviors through hierarchical structuring[20–21]. While traditional wettability studies have focused on Young's equation for ideal flat surfaces, real surfaces possess roughness that fundamentally alters liquid-solid interactions. Super-hydrophilic surfaces, characterized by water contact angles approaching zero, offer enhanced water capture and spreading capabilities that are particularly valuable for moisture sensing applications. Recent advances in hierarchical surface design have demonstrated that multi-scale roughness can amplify the intrinsic hydrophilicity of oxide materials, leading to rapid water adsorption kinetics and improved sensor response times.

Al-based hierarchical surfaces have been fabricated through various methodologies including chemical etching[22–26], anodic oxidation[27–29], and hydrothermal treatment to produce boehmite [AlO(OH)] nanostructures[30–40]. Anodization provides systematic control over nanoscale porosity and surface chemistry through manipulation of current density, electrolyte composition, and reaction time, while post-anodization treatments enable further structural and chemical modifications. Most previous investigations have emphasized super-hydrophobic Al-based coatings for applications including self-cleaning[40], anti-icing[36], and corrosion resistance[34–35]. In contrast, despite the intrinsic hydrophilicity of both Al_2O_3 and AlO(OH) arising from abundant surface hydroxyl groups, the development of super-hydrophilic hierarchical Al surfaces for vapor- and liquid-phase moisture-responsive applications remains relatively unexplored.

The dual functionality of super-hydrophilic hierarchical surfaces for both moisture gettering and moisture sensing represents a significant opportunity for advanced MEMS applications. In the aqueous regime, rapid capillary wetting and complete water spreading can enhance moisture removal efficiency for gettering applications. Simultaneously, in the vapor regime, enhanced water adsorption-desorption kinetics can improve sensor sensitivity and response speed for real-time humidity monitoring. The integration of hierarchical Al_2O_3 structures with silicon MEMS platforms could enable multifunctional devices capable of both passive moisture control and active environmental sensing.

In this study, we demonstrate the fabrication of super-hydrophilic hierarchical surfaces composed of nanoporous Al_2O_3 and AlO(OH) on micro-textured silicon wafers through controlled anodization and post-treatment processes. Silicon substrates were pre-textured via alkaline etching to create micron-scale pyramidal structures, followed by Al film deposition, one-step anodization to form porous AAO, and subsequent pore-widening, thermal annealing, or hot-water treatment. The resulting oxide architectures exhibit near-zero water contact angles in the aqueous regime and pronounced H_2O adsorption-desorption responses in the vapor regime. These complementary behaviors—rapid capillary wetting and multilayer vapor adsorption—support the potential application of hierarchical oxide/Si interfaces as interactive water-affine surfaces for both moisture gettering and chemosensing applications. Comprehensive characterization through thermogravimetric analysis, moisture isotherms, infrared spectroscopy, and contact angle

 doi:10.20944/preprints202509.1977.v1

measurements elucidates the relationship between hierarchical structuring, surface chemistry, and water affinity mechanisms.

2. Materials and Methods

2.1. Anodizing and Pore Widening of Al

Al foils (0.13 mm thick, 99.99% purity; Sigma-Aldrich) were degreased in acetone, rinsed with deionized (DI) water, and etched in 0.1 M sodium hydroxide (NaOH) until bubbling appeared to remove the native oxide. Samples were rinsed several times in DI water and dried in air at 27 °C. AAO templates were prepared using a standard two-step anodization process (Figure 1). Pre-cleaned Al foils were mounted in a customized jig, exposing a 25 mm-diameter area, and first-anodized at 50 V in 0.3 M oxalic acid at 20 °C for 10 min under magnetic stirring. The oxide layer was then removed by immersing in 1.8 wt% chromic acid and 6 wt% phosphoric acid for 5 h at 27 °C, leaving an ordered pattern on the Al surface. The pre-patterned foils were anodized again under the same conditions for 7 h 30 min. Residual Al beneath the porous alumina was removed by wet etching in 0.1 M copper(II) chloride ($CuCl_2$) and 20 vol% hydrochloric acid (HCl) for 1 h, and unopened alumina was removed with 5 wt% phosphoric acid. To investigate the effect of pore widening on moisture adsorption, pore-widening was performed for 0, 1, and 2 h.

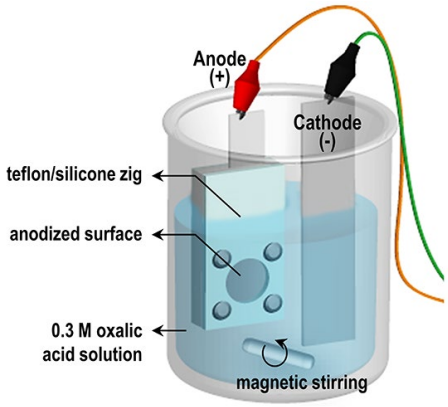

Figure 1. Schematic illustration of experimental set-up of anodization.

2.2. Synthesis of AAO Film on Textured Silicon Substrates

Texturing was performed using an alkaline solution containing 2 wt% tetramethylammonium hydroxide (TMAH) and 8 wt% isopropyl alcohol (IPA)[41,42]. IPA aided in removing hydrogen bubbles, promoting uniform etching[43]. Before texturing, p-type Si wafers were dipped in 10% hydrofluoric acid (HF) to remove native oxide, rinsed twice in DI water, and etched at 65–85 °C for 20 or 30 min to produce micro-pyramidal textures of varying sizes. A 1 μm-thick high-purity Al film was deposited on the textured Si wafers by e-beam evaporation without an adhesion layer to avoid affecting moisture adsorption. The Al-coated wafers were mounted on copper tape using silver paste (Ted Pella, Inc.), insulated with polyimide tape, and anodized in 0.3 M oxalic acid at 20 °C under 20 V for 100–800 s in a two-electrode setup. Current density–time transients were recorded and compared to those from Al foils. Pore widening was subsequently carried out in 5 wt% phosphoric acid at 24–27 °C for 20–80 min, following the same procedure as for freestanding AAO.

 doi:10.20944/preprints202509.1977.v1

2.3. Surface Treatments: Pore Widening, Annealing, and Boiling-Water Conversion

Pore widening was also performed using a solution of 1.8 wt% chromic acid and 6 wt% phosphoric acid at 24–27 °C for 20–80 min, ensuring that structural collapse did not occur. To study the effect of other post-treatments, porous AAO/Si specimens anodized for 10 min and pore-widened for 40 min were subjected to further modifications. Thermal annealing was conducted in air at 600 °C, 800 °C, or 1,220 °C for 5 h to induce phase transitions from γ- to α-Al_2O_3. Separately, AAO on flat and textured Si was immersed in boiling water (70–80 °C) for 10 min to form boehmite [AlO(OH)]; this time was optimized based on morphology. Finally, all hierarchical surfaces were treated with 0.5 % (1H,1H,2H,2H-Perfluorooctyl)trichlorosilane (PFOTS) in n-hexane for 10 min and oven-dried at 150 °C for 1 h.

2.4. Characterization

Surface morphology was examined by scanning electron microscopy (SEM, Hitachi S-4800) equipped with energy-dispersive spectroscopy (EDS). Crystalline phases were identified by X-ray diffraction (Rigaku D/max 2400). Static water contact angles (CA) were measured at room temperature with a horizontal microscope and protractor eyepiece, using five droplets per sample. Cross-sections were prepared by diamond cutting and imaged by SEM. Thickness and porosity were measured from SEM images using Image Tool software. Thermogravimetric analysis (TGA, PerkinElmer TGA-7) was performed in argon from 30 °C to 1,300 °C at 10 °C/min with 20 mL/min gas flow. Moisture adsorption/desorption isotherms were collected at 25.15 °C and 0–95% RH (BELSORP-aqua3, BEL Japan) after pre-dehydration at 300 °C for 24 h. RH was defined as p/p_0, where p is the partial pressure of water vapor and p_0 its saturation pressure at 25.15 °C. Infrared spectra were recorded using a Nicolet iS10 FTIR after moisture adsorption and evacuation to 10% RH at room temperature.

3. Results and Discussion

3.1. Anodizing of Al Foil and Al on Textured Silicon Wafers

Figure 2 schematically illustrates the anodization process forming porous AAO films and the corresponding current density–time transients. As shown in Figure 2a, anodizing freestanding Al foil produces a typical current density profile characteristic of the two-step mild anodization process, involving the formation and growth of a nanoporous oxide layer[43, 44]. In contrast, anodizing a 1 μm Al layer on textured Si resulted in an abrupt rise in current density after ~520 s (Figure 2b). This increase indicates the depletion of Al and the exposure of the underlying Si surface, shifting the reaction environment from 'AAO/oxalic acid' to 'Si/oxalic acid'. Although current typically decreases as an oxide barrier forms, the electric field concentration on the textured surface likely accelerates water dissociation and oxygen bubble generation, detaching the AAO layer from the Si substrate[45]. (No adhesion layer was used, as noted in the Methods.) The anodizing time for Al/Si samples was therefore optimized to prevent delamination.

 doi:10.20944/preprints202509.1977.v1

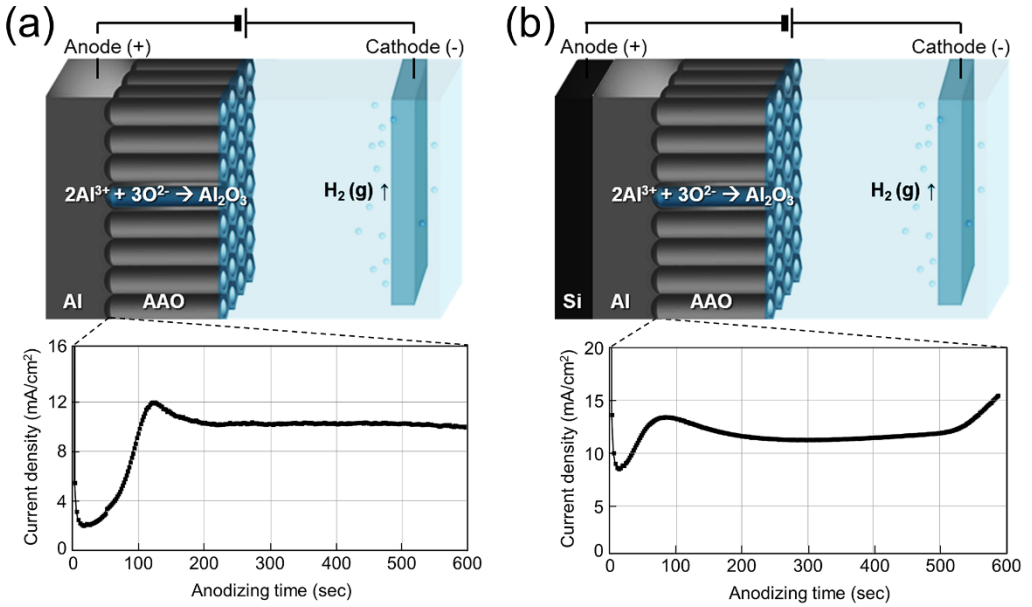

Figure 2. Schematic illustration of the anodizing mechanism of (a) freestanding 60 μm Al foil and (b) 1 μm Al deposited on Si wafer, with corresponding current density–time transients over 600 s.

3.2. Fabrication of Freestanding AAO Films from Al Foil and Their Water Vapor Adsorption Characteristics

To evaluate the moisture adsorption capacity of AAO, we first fabricated freestanding AAO films using a well-established two-step anodization method[46] (Figure 3). Figure 3a outlines the process flow: high-purity Al foil was first anodized to form a disordered oxide layer, which was then selectively dissolved to expose the pre-patterned Al surface beneath. Subsequent second anodization produced a uniform nanoporous structure, followed by wet etching of the residual Al and pore widening (0–2 h) to yield freestanding AAO membranes. SEM images (Figure 3b–f) show the morphological evolution through these steps. The as-received Al foil exhibited a rough, featureless surface (Figure 3b), and the initial anodized surface showed irregular pores without clear ordering (Figure 3c). During chemical dissolution of the first AAO, preferential etching of protruding regions smoothed the surface while exposing emerging pores (Figure 3d). After complete removal of the initial oxide, the underlying Al surface displayed embossed hemispherical nano-patterns (Figure 3e), formed by mechanical stresses and ~1.2× volume expansion during anodization, which promote pore self-ordering[47]. These patterns guided the growth of vertically aligned channels during the second anodization, resulting in a transparent, hexagonally ordered AAO template (Figure 3f,g).

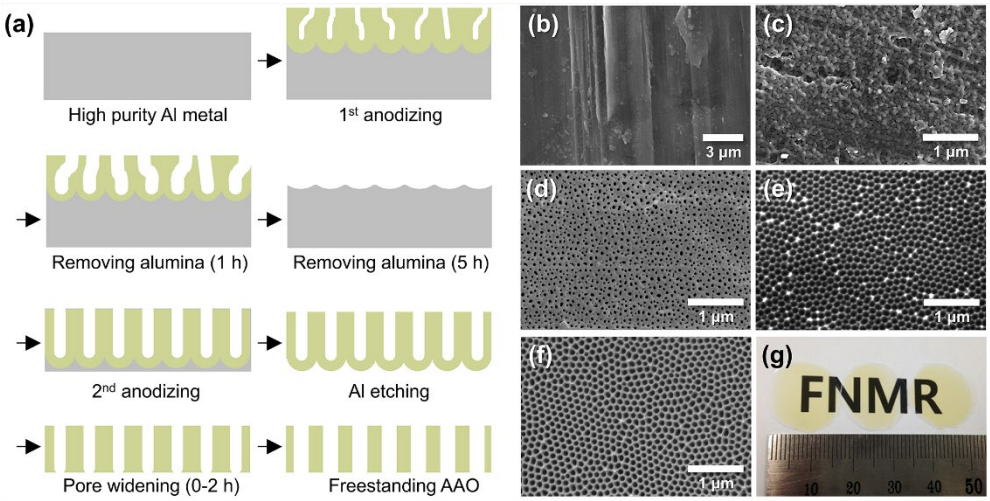

 doi:10.20944/preprints202509.1977.v1

Figure 3. Schematic of the fabrication process for freestanding AAO films. (b–f) SEM images showing morphological evolution: (b) as-received Al foil, (c) disordered Al_2O_3 after first anodization at 20 V for 10 min in 0.3 M oxalic acid, (d) partially dissolved porous Al_2O_3 after etching in 1.8 wt% chromic acid and 6 wt% phosphoric acid at 27 °C for 1 h, (e) pre-patterned Al surface after complete oxide removal, and (f) freestanding AAO obtained after Al removal and 1 h pore widening. (g) Optical image of the freestanding AAO shown in (f).

The pore-widening process was systematically examined by varying immersion time (0–2 h, Figure 4). As-prepared AAO showed 22% porosity and retained a barrier layer blocking one side of the columnar pores (a,d). With increasing immersion time, the barrier layer dissolved and the pores widened progressively, reaching 45% porosity at 1 h and 49% after 2 h (b–f). While the bottom-side pores opened gradually, the top-side pores—already exposed to acid—expanded continuously. All samples retained well-defined hexagonal cell ordering throughout the pore-widening process.

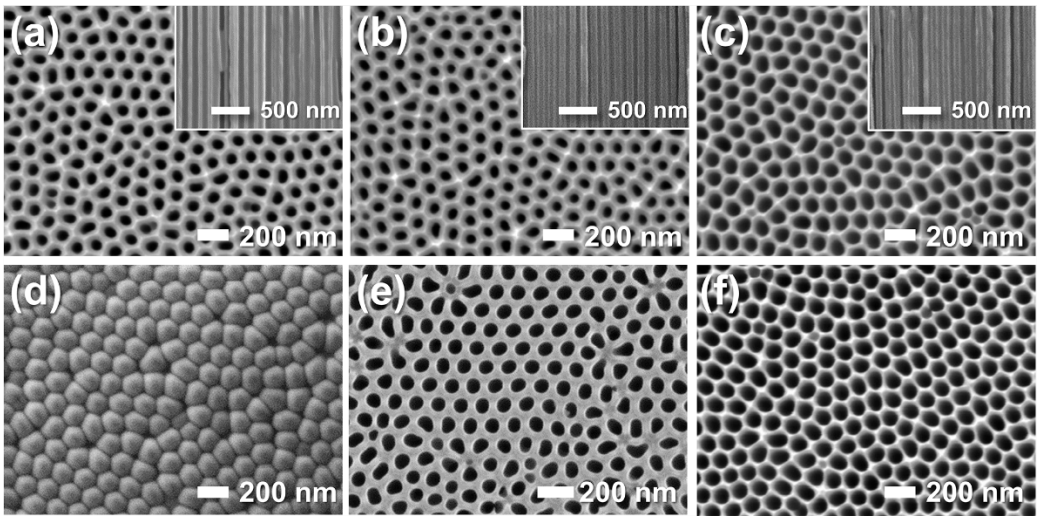

Figure 4. FE-SEM images of the (a–c) top and (d–f) bottom surfaces of AAO membranes before (a,d) and after pore-widening in 5 wt% phosphoric acid (H_3PO_4) for (b,e) 1 h and (c,f) 2 h. Insets show cross-sectional views.

The influence of AAO surface properties on moisture adsorption was examined using TGA and moisture adsorption–desorption isotherms (Figure 5). The TGA profiles (Figure 5a) reveal four characteristic stages: stage 1, adsorption; stage 2, dehydration; stage 3, dehydroxylation; and stage 4, thermal decomposition. The expanded stage 1 region (30–150 °C) is shown in Figure 5b. The sample mass increased up to ~60 °C, likely due to the adsorption of residual gases on the AAO surface. This behavior contrasts with the steady ~4% mass loss up to 400 °C in air reported by Mata-Zamora et al.[48]. The observed weight gain can be attributed to the adsorption of residual gases in argon (Ar) carrier gas, where surface hydroxyl groups may promote hydration layer formation and trap contaminants. This is supported by the subsequent return of the mass to its initial value at 510–556 °C, slightly above the typical dehydration (~400 °C, stage 2) and dehydroxylation (~700 °C, stage 3) temperatures[49]. At higher temperatures (stage 4), the mass loss is consistent with the thermal decomposition of oxalate anions and the crystallization of amorphous AAO to γ-Al_2O_3 at ~903 °C and to α-Al_2O_3 at ~1219 °C[50].

 doi:10.20944/preprints202509.1977.v1

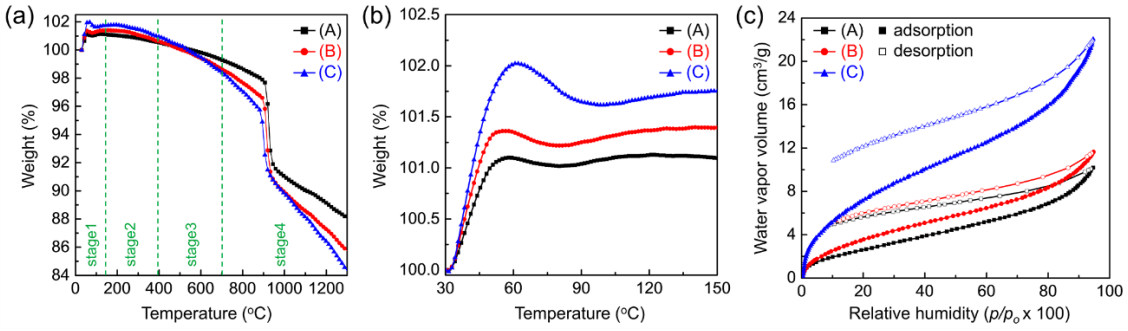

Figure 5. Effect of pore-widening on the moisture adsorption behavior of AAO. (a) Thermogravimetric analysis (TGA) curves of AAO membranes (A: as-prepared, B: pore-widened 1 h, C: pore-widened 2 h) measured in flowing argon (Ar) at 10 °C min^{-1}, showing four characteristic stages: stage 1, adsorption; stage 2, dehydration; stage 3, dehydroxylation; and stage 4, thermal decomposition. (b) Expanded view of stage 1 (30–150 °C) showing weight gains due to residual gas adsorption on surface hydroxyl sites. (c) Moisture adsorption–desorption isotherms measured at 25 °C, showing increased water vapor uptake with prolonged pore-widening (porosity: 22 % → 49 %).

The moisture adsorption–desorption isotherms measured at 25 °C are shown in Figure 5c. Because adsorption depends not only on vapor pressure but also on the amount of water pre-bound to the surface[14], all AAO samples were pre-heated to 300 °C and held under vacuum for 24 h. All isotherms exhibit type II behavior in the Brunauer classification, indicative of multilayer adsorption[51]. Adsorption rose steeply at low relative humidity (RH < 10%), then increased gradually until capillary condensation occurred at high RH (> 80%). The monolayer capacity, calculated from the isotherms, was 12–15% RH—between those reported for single-crystalline (0001) and polycrystalline α-Al_2O_3 (10% and 17% RH, respectively)[51]—consistent with dissociative chemisorption forming a molecular monolayer of water[51, 52, 53, 54].

This behavior can be explained by the presence of unsaturated surface Al cations acting as Lewis acid sites, which first physically adsorb and orient water molecules, then dissociate them into H and OH to form surface hydroxyl groups[13, 54, 56]. These hydroxyl groups establish a hydrogen-bonded monolayer that gradually evolves into multilayers as coverage increases. With increasing water coverage, the heat of adsorption decreases and surface accessibility is reduced[54]. Although surface effects diminish, strongly hydrogen-bonded hydrates can still form at the interface (2–3 water molecules at room temperature, tetrahedral networks at cryogenic temperatures). At intermediate RH (10–80%), adsorption increased steadily, suggesting the growth of ice-like ordered multilayers through hydrogen bonding to hydroxylated surfaces[57]. The data show the formation of an actual monolayer and up to three multilayers near 75–85% RH. The observed hysteresis between adsorption and desorption curves for all pore sizes further supports partial irreversible binding of water, reflecting chemisorption behavior.

The overall adsorption capacity increased across the full p/p_0 range as the pores were widened. At RH = 20%—a condition directly relevant to moisture getter performance—the capacity rose from 2.66 to 7.30 $cm^3\ g^{-1}$ as porosity increased from 22% to 49%. The corresponding monolayer capacities were 2.08 $cm^3\ g^{-1}$ and 5.87 $cm^3\ g^{-1}$, respectively. This enhancement reflects not only increased porosity but also enrichment of surface functional groups. AAO has a hexagonal structure with compositional gradients: an outer amorphous layer, an intermediate partially crystalline layer, and an inner highly crystalline framework[58-60]. During anodization, anionic species such as oxide ion (O^{2-}), superoxide ion (O^-), and oxalate can be incorporated into the amorphous regions (up to ~5% of the oxide)[61]. These anionic impurities, once exposed to the surface by pore widening, can act as additional adsorption sites, forming strong hydrogen bonds with water molecules[52, 62]. This explains why acidic pore-widening treatments significantly enhance the water-gettering performance of AAO by increasing both porosity and the density of active adsorption sites.

 doi:10.20944/preprints202509.1977.v1

The FT-IR spectra of AAO with different porosities are shown in Figure 6. Consistent with the conditions used for the moisture adsorption–desorption isotherm measurements, all spectra were collected after equilibrating at 10% RH. In agreement with previous reports[61, 63], distinct peaks from isolated hydroxyl groups (3800–3670 cm^{-1}) were not observed. Instead, broad bands appeared at 3556–3440 cm^{-1}, corresponding to hydrogen-bonded hydroxyls on AlO(OH) surfaces[64]. This reflects the susceptibility of the amorphous regions of AAO to structural rearrangement upon exposure to water, which promotes the formation of boehmite-like phases[65, 66]. A broad O–H stretching band spanning 3500–3000 cm^{-1} indicates physically adsorbed H_2O, consistent with rapid multilayer water film formation on a hydrogen-bonded monolayer as inferred from the isotherm data. The band at 1630 cm^{-1} is attributed to water confined within the pores, while a strong feature between 1550–1480 cm^{-1} corresponds to oxalate anions incorporated into the oxide (up to ~5% of the anodized volume)[52, 61]. These anions can act as basic sites for hydrogen bonding with water molecules[52]. Additionally, a broad absorption near 1100 cm^{-1} was observed, corresponding to O–H bending vibrations[67].

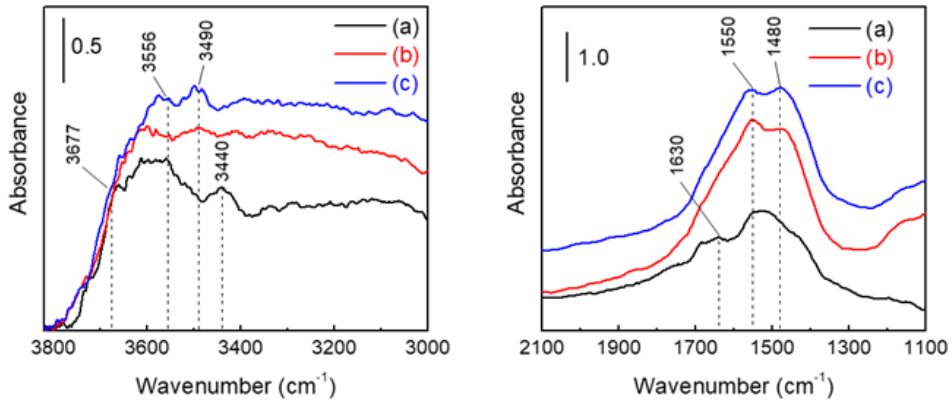

Figure 6. FT-IR spectra of AAO membranes (a) as-prepared and after pore-widening for (b) 1 h and (c) 2 h. All spectra were recorded after moisture adsorption and evacuation to 10% RH at room temperature.

3.3. Fabrication of AAO on Textured Silicon Wafers

To explore the integration of AAO with MEMS, we fabricated AAO layers on p-type Si wafers with post-treatments, aiming to develop moisture gettering and sensing platforms (Figure 7). To enhance adsorption probability, micron-scale pyramid textures were first formed on the Si surface using a TMAH-based etchant compatible with standard MEMS processes (Figure 8). The pyramid size increased with higher etching temperature and time, ranging from 0.27 ± 0.1 μm (65 °C, 20 min) to 2.1 ± 1.1 μm (85 °C, 30 min). A 1 μm-thick Al film was then deposited by e-beam evaporation on the textured Si surface with larger pyramids (~2.1 μm) to provide sufficient getter and sensor material thickness. Subsequent anodization produced conformal AAO layers under various reaction times, followed by pore-widening treatments under different durations to tailor the hierarchical structure. Representative FE-SEM images of the AAO layer anodized for 10 min and pore-widened for 40 min are shown in Figure 7.

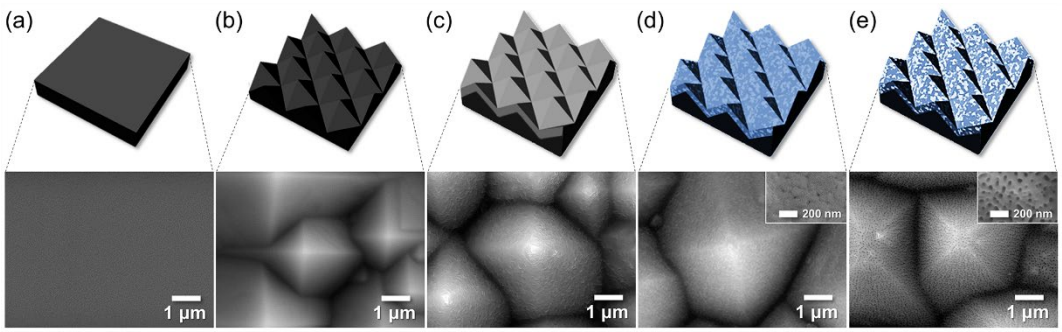

 doi:10.20944/preprints202509.1977.v1

Figure 7. Schematics and FE-SEM images of the stages of fabrication of AAO layer on textured Si wafer; (a) a bare Si wafer, (b) textured Si (t-Si), (c) e-beam evaporated 1-µm-thick Al, and AAO film on the textured Si (d) as-anodized for 10 min and then (e) pore-widened for 40 min.

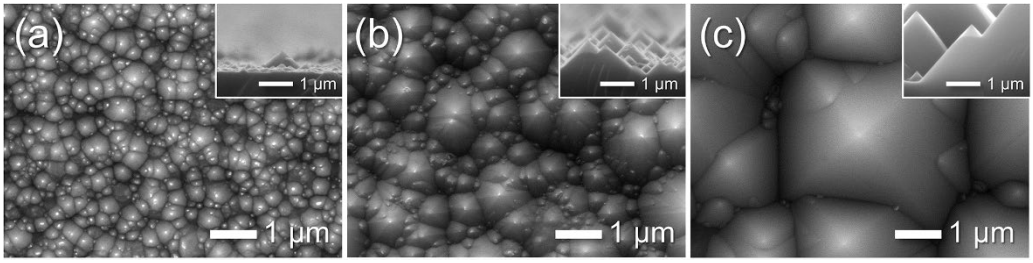

Figure 8. FE-SEM images of textured Si substrate in the alkaline solution containing 8 wt% TMAH and 2 wt% IPA etched for different times at varying temperatures; (a) 20 min at 65°C, (b) 20 min at 75°C, and (c) 30 min at 85°C.

Figure 9a–f shows cross-sectional FE-SEM images taken near the AAO/Si interface after anodization for 500–700 s. All samples were subjected to a fixed 40 min pore-widening treatment to produce a porous structure. The AAO thickness measured from these cross-sections is plotted as a function of anodizing time in Figure 9g. The thickness increased linearly (growth rate ≈ 1.4 nm s^{-1}), consistent with the ordered hexagonal pore growth regime. After 700 s, residual Al was completely removed, and the interface morphology confirmed full conversion to AAO. However, Figure 9g also shows a sudden decrease and large variation in thickness between 600–800 s. This instability arises when the Al layer becomes fully consumed and the acidic electrolyte reaches the underlying Si, generating oxygen bubbles that detach the AAO film from the textured substrate (Figure 9f)[45]. Based on this behavior, the anodizing time for subsequent experiments was fixed at 600 s, just before the onset of this detachment regime.

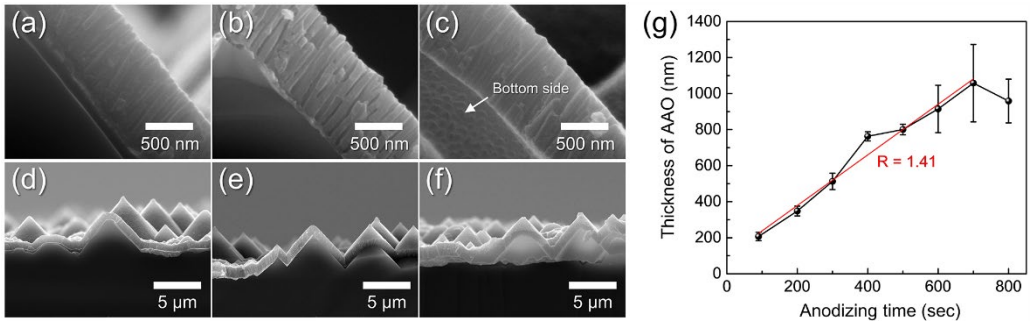

Figure 9. Cross-sectional FE-SEM images of AAO layers formed on t-Si by anodization for (a,d) 500 s, (b,e) 600 s, and (c,f) 700 s, shown at high (a–c) and low (d–f) magnification. (g) AAO thickness as a function of anodizing time. All samples were pore-widened for 40 min in 1.8 wt% chromic acid and 6 wt% phosphoric acid after anodization.

3.4. Vapor and Aqueous-Phase H_2O Responses of Hierarchical AAO/t-Si Surfaces

Figure 10a–d shows the surface morphology of AAO/Si structures after pore widening for 40–130 min. The measured pore diameter, porosity, and film thickness are summarized in Figure 10e. Pore diameter and porosity increased with pore-widening time, reaching 89.5 ± 18.4 nm and 37.2%, respectively, consistent with the trend observed for freestanding AAO. Because the AAO was formed by a single-step anodization of a thin e-beam-deposited Al layer, the surface pores were less ordered, and the porosity increase was more gradual compared with freestanding AAO.

 doi:10.20944/preprints202509.1977.v1

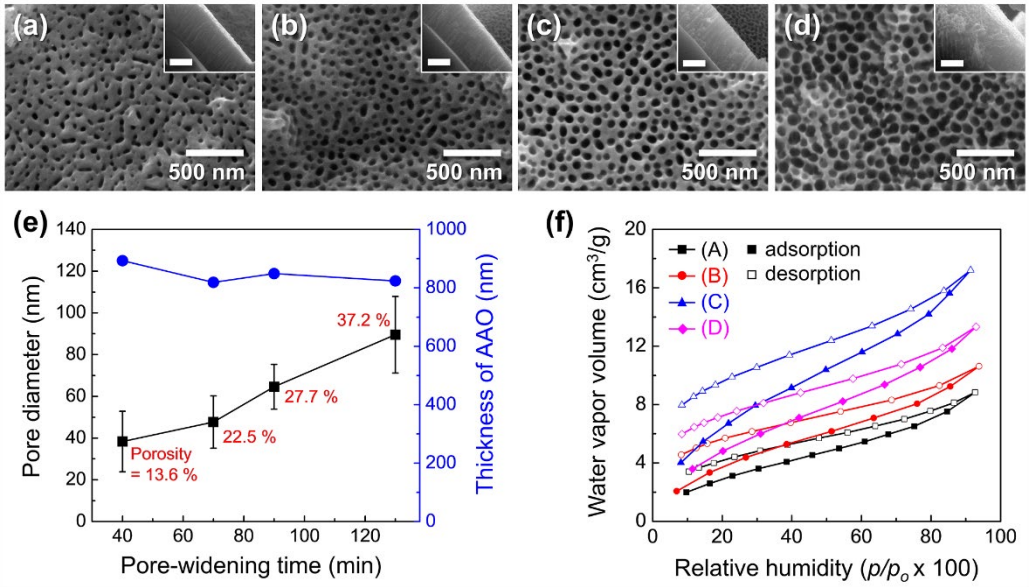

Figure 10. FE-SEM images of AAO surfaces on t-Si after pore widening for (a) 40, (b) 70, (c) 90, and (d) 130 min. Insets show corresponding cross-sectional views (scale bars: 500 nm). (e) Pore diameter (black) and film thickness (blue) as a function of pore-widening time; porosity values are indicated in red. (f) Moisture adsorption–desorption isotherms measured at 25 °C for samples with different porosities: (A) 13.6%, (B) 22.5%, (C) 27.7%, and (D) 37.2%.

Moisture adsorption–desorption isotherms for samples with different porosities are shown in Figure 10f. Adsorption capacity increased with porosity, reflecting the combined effects of higher surface area and more available binding sites. A marked rise in adsorption was observed as porosity increased from 22.5% to 27.7%, suggesting that exposed anionic impurities on the AAO surface serve as additional adsorption sites for H_2O. The water vapor uptake at 20% RH peaked at 6.42 $cm^3\ g^{-1}$ at 27.7% porosity, but decreased to 4.85 $cm^3\ g^{-1}$ at 37.2% despite the higher porosity. This reduction is attributed to structural collapse of the brittle pore walls after 130 min of pore widening, accompanied by an ~8% decrease in oxide thickness. Such brittleness could impair adsorption performance and generate particulate debris in MEMS devices.

Overall, these results indicate that acidic pore-widening is an effective strategy to enhance the water-gettering capacity of AAO, but immersion time must be carefully optimized to avoid structural damage, getter loss, and contamination.

Figure 11a,b show the surface morphologies and WCAs of Al/f-Si and porous AAO/f-Si prepared by one-step anodization followed by 60 min pore widening. The Al/f-Si surface exhibited a WCA of 57°, while the nano-porous AAO/f-Si surface showed a reduced WCA of 38°. Although native oxidized Al is generally hydrophilic (reported WCAs of ~67°[7] or ~33°[12] after electropolishing), the lower WCA observed here likely arises from nano-scale roughness formed during e-beam evaporation. During anodization, a porous oxide layer formed on the Al surface, introducing hydroxyl groups that contribute to enhanced wettability[13, 18, 54, 68]. Thus, anodization can be considered an effective strategy to regulate the wetting behavior of Al surfaces by combining nano-scale porosity and surface chemical modification. However, these surfaces remain above the threshold for super-hydrophilicity (WCA ≈ 0°).

To further investigate the effect of micro-scale texturing, porous AAO layers were formed on small- and large-pyramid t-Si substrates under the same anodization and pore-widening conditions (Figure 11c,d). These hierarchical AAO/t-Si surfaces showed WCAs of 6° and 5°, respectively—effectively super-hydrophilic and within experimental error of each other. This strong decrease in WCA can be explained by Wenzel's equation ($\cos\theta_w = r\cos\theta$), where increasing the roughness factor r amplifies the intrinsic wettability of a surface with $\theta < 90°$[70, 71]. The results demonstrate that combining nano-porous AAO with micro-textured Si dramatically enhances surface hydrophilicity,

 doi:10.20944/preprints202509.1977.v1

enabling near-complete water spreading. Similar behavior was reported by Leem et al. [72], who observed super-hydrophilic (< 5°) wetting on Si surfaces with combined nano/micro textures produced by KOH-based wet etching and ICP etching, confirming the critical role of micro-scale texture in achieving extreme wettability.

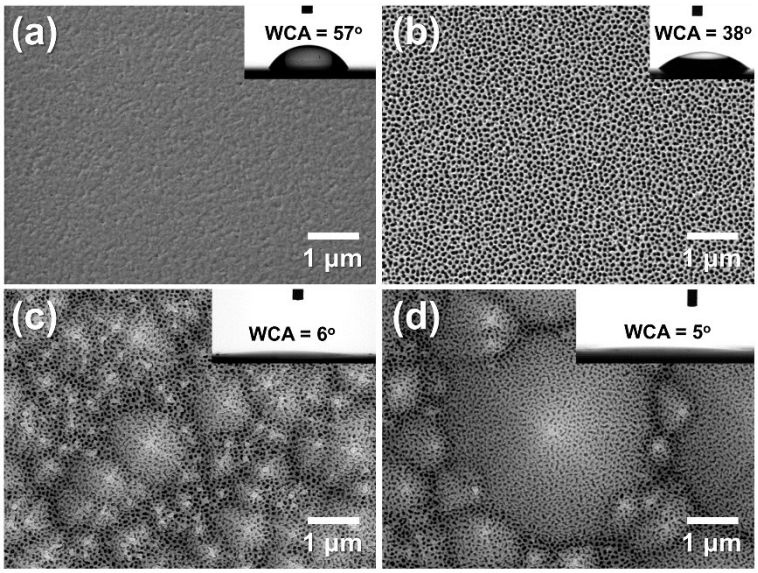

Figure 11. FE-SEM images of (a) as-deposited Al on flat Silicon (f-Si), and AAO films formed on (b) f-Si, (c) small-textured Si (t-Si), and (d) large-textured Si (t-Si). All samples were anodized for 175 s at 20 °C in 0.3 M oxalic acid and pore-widened for 60 min in 1.8 wt% chromic acid and 6 wt% phosphoric acid. Insets show water contact angles (WCAs).

To investigate nanoscale morphological evolution, AAO/t-Si samples (prepared on pre-textured Si etched at 85 °C for 30 min) were subjected to pore-widening treatments for 20–80 min. As shown in Figure 12a–c, increasing immersion time enlarged the pore diameter and porosity. After 80 min, the pore sidewalls were heavily etched, leaving a wire-like framework composed of Al_2O_3 with an atomic ratio of Al:O ≈ 47:53 (Figure 12e). Further etching beyond 80 min caused the fragile nanowires to collapse and detach from the surface (not shown).

Figure 12d shows the change in WCA with pore-widening time. The as-anodized surface exhibited a CA of 72° ± 8°, which sharply decreased to 3° ± 2° after 20 min and remained near this value (5° ± 3°) beyond 40 min. This dramatic WCA reduction is attributed to the formation of a nano-porous oxide layer atop the micro-textured substrate, which increases surface roughness at the nanoscale. Similar trends have been reported by Ye et al. and Kim et al. for AAO prepared in phosphoric acid[54] and oxalic acid at 65 V[28], respectively. In contrast, Buijinsters et al.[29] showed that AAO films with much larger pores (140–190 nm) and ~60% porosity exhibit increased hydrophobicity (WCA up to 128°), indicating that pore geometry critically influences wettability.

Interestingly, wettability continued to improve slightly between 60–80 min despite no further decrease in WCA, coinciding with the development of a porous binary structure composed of nanowires and nanopores. The super-hydrophilicity of these wire-like Al_2O_3/t-Si surfaces cannot be explained by Wenzel's equation, which becomes invalid when $\cos\theta \approx 1$ ($r \gg 1$). Instead, it is better described by the three-dimensional capillary effect[75]. Through wicking and imbibition, water rapidly spreads within the hierarchical structure, forming a thin solid–liquid composite film characteristic of super-hydrophilic surfaces. These results align with previous reports of capillary-driven super-hydrophilicity in broken-sheet and nanoporous structures[27, 28].

 doi:10.20944/preprints202509.1977.v1

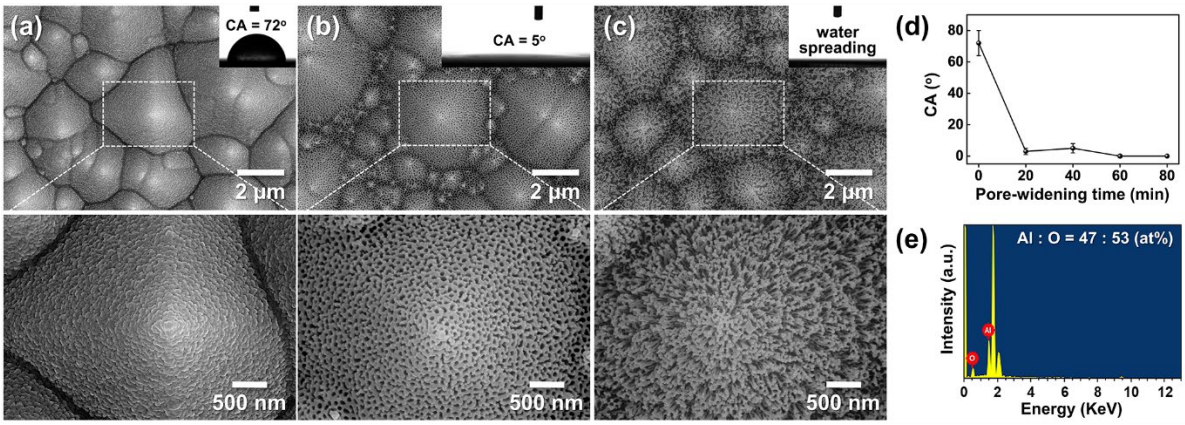

Figure 12. (a–c) Top-view SEM images of AAO on t-Si: (a) as-anodized in 0.3 M oxalic acid at 50 V and 20 °C for 175 s, and after pore widening in 1.8 wt% chromic acid + 6 wt% phosphoric acid at 27 °C for (b) 40 min and (c) 80 min. Insets show corresponding WCAs. (d) WCAs as a function of pore-widening time. (e) Energy-dispersive spectroscopy (EDS) spectrum of the wire-like structure in (c), showing an Al:O atomic ratio of 47:53.

Figure 13a–c shows the morphological evolution of AAO/t-Si after calcination at 600–1,220 °C, and Figure 13d,e present the corresponding phase composition and WCAs. XRD analysis revealed that the initially amorphous AAO transformed into γ-Al_2O_3 at 800 °C and further into α-Al_2O_3 above 1,220 °C. The as-anodized amorphous surface exhibited a WCA of 72° ± 8°, which slightly increased to 85° ± 15° after calcination at 600 °C, indicating weak hydrophobic behavior. This can be attributed to trapped air pockets within the porous structure, consistent with the Cassie–Baxter model[77, 78]. Upon heating to 800 °C, the WCA abruptly dropped to near 0°, despite the surface retaining a mottled morphology without apparent structural collapse, suggesting the formation of metastable γ-Al_2O_3 mixed with amorphous domains. At 1,220 °C, thermodynamically stable α-Al_2O_3 was obtained, showing smoothened surfaces except for occasional protrusions at pyramid tips (Figure 13c inset), likely due to surface atomic migration filling the inverted pyramid regions. This smooth α-Al_2O_3 surface also exhibited WCAs close to 0°. The sharp transition from hydrophobic to super-hydrophilic wetting cannot be explained solely by surface roughness, indicating a role of surface chemistry.

Amorphous AAO/t-Si showed high variability in WCA (>65°) due to its unstable nature and susceptibility to conversion into boehmite, which reduces surface area and porosity[65, 66]. Considering the sessile droplet method is highly sensitive to local heterogeneity, such variations are reasonable[79]. In contrast, both γ- and α-Al_2O_3 phases are known to present higher densities of hydroxyl groups and active sites than the amorphous phase[80, 81], leading to enhanced surface hydrogen bonding with H_2O. Thoroughly cleaned α-Al_2O_3 films have reported WCAs < 5°[82], consistent with the present results. These findings demonstrate that calcination can convert porous amorphous AAO into super-hydrophilic γ- or α-Al_2O_3 by increasing surface energy through crystallization and hydroxylation. However, the high temperatures required (>800 °C) may limit compatibility with existing device manufacturing environments.

 doi:10.20944/preprints202509.1977.v1

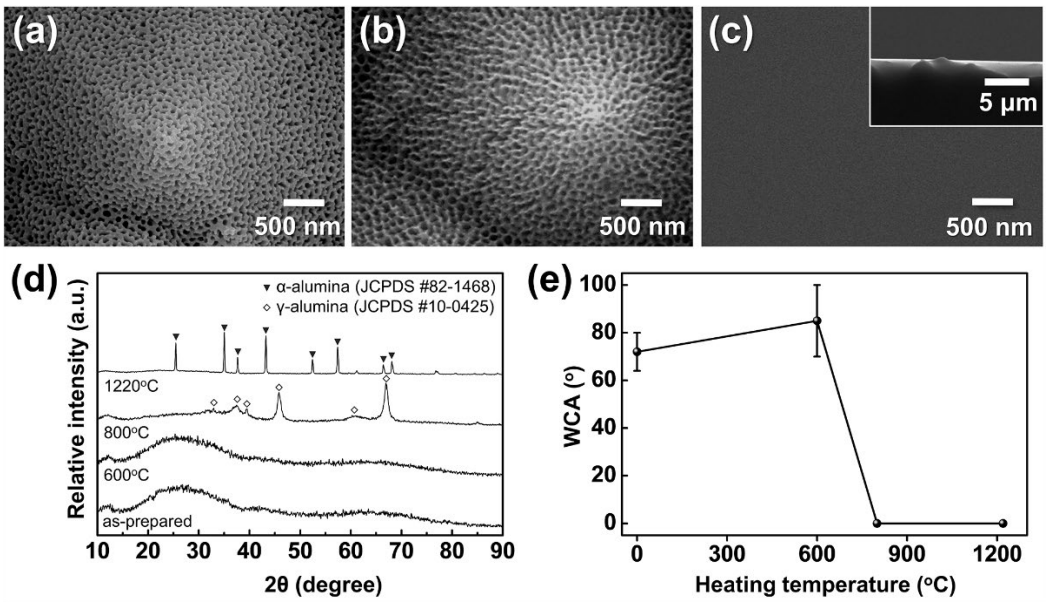

Figure 13. FE-SEM images of AAO on t-Si calcined for 5 h at (a) 600 °C, (b) 800 °C, and (c) 1,220 °C (inset: cross-sectional view of (c)); (d) XRD patterns of AAO after calcination under the same conditions; and (e) WCAs measured before and after calcination.

Building on the preceding investigations of surface roughness and crystallinity effects, we further examined how surface functionalization contributes to wettability by inducing hydroxyl-rich phases through hot-water treatment (boehmitization). Figure 14 shows the morphological evolution of porous AAO/t-Si after immersion in boiling water (≈100 °C) for different times. After 2 min, the nanopores began to seal and small hydrate nanoparticles appeared on the surface (Figure 14b). Immersion for 5 min led to the emergence of flake-like structures, often described as flower- or petal-like, which progressively grew into dense sheet-like networks as immersion time increased to 10 and 15 min (Figure 14c–e).

This transformation aligns with previous reports that Al, Al alloys, and Al_2O_3 rapidly form hydrated oxide layers containing abundant hydroxyl (–OH) groups when exposed to hot water (50–100 °C)[83-85]. The initial reaction produces loosely packed $Al_2O_3 \cdot xH_2O$ and hydrogen gas, generating nanoscale capillary pores[33]Continued reaction with H_2O converts this layer into crystalline boehmite [AlO(OH)][87]. The growth of hydroxide/boehmite nanostructures increases both the surface roughness and the density of surface hydroxyl groups, thereby enhancing surface energy and imparting super-hydrophilic character[33, 34, 89]. Collectively, the SEM images indicate that the hierarchical porous film obtained after the optimized 10 min immersion consists of a mixed hydroxide–boehmite network enriched with hydroxyl groups, which likely underlies its strong water affinity.

 doi:10.20944/preprints202509.1977.v1

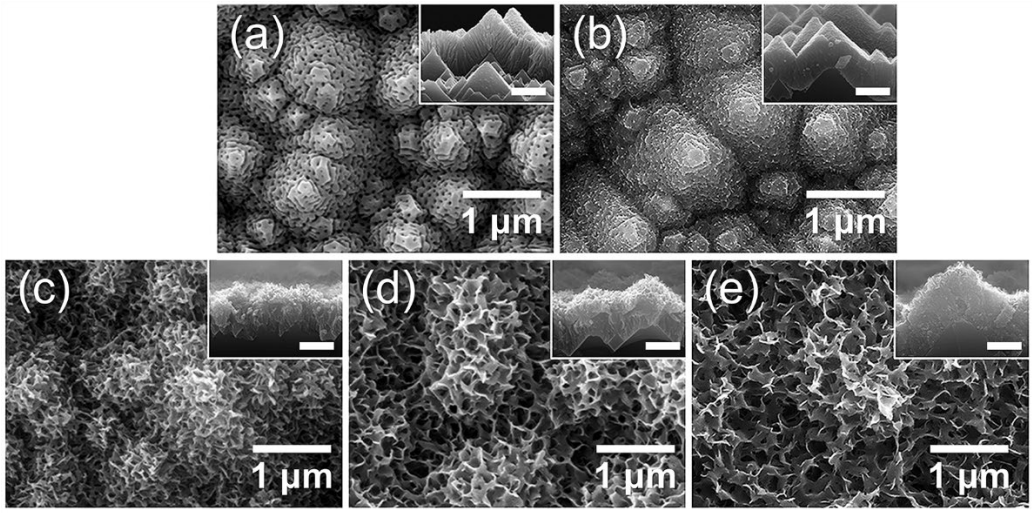

Figure 14. FE-SEM images of top views and cross-sectional insets of AAO on t-Si: (a) as-prepared and after immersion in boiling water for (b) 2 min, (c) 5 min, (d) 10 min, and (e) 15 min.

Figure 15a,b show the morphological evolution after 10 min immersion in boiling water. The flat AAO/Si developed uniform petal-like AlO(OH) structures of 50–300 nm, whereas the hierarchical t-Si substrate produced multi-scale architectures composed of micro-pyramids covered by slightly curled nanosheets. Despite both surfaces appearing hydrophilic, the WCAs revealed a striking contrast: 23° on flat AlO(OH)/Si versus complete water spreading (≈0°) on hierarchical AlO(OH)/t-Si. This dramatic enhancement arises from two synergistic factors: the abundant surface hydroxyl groups formed during boehmitization, which strongly hydrogen-bond with H_2O, and the capillary-driven imbibition enabled by the hierarchical micro/nano structure.

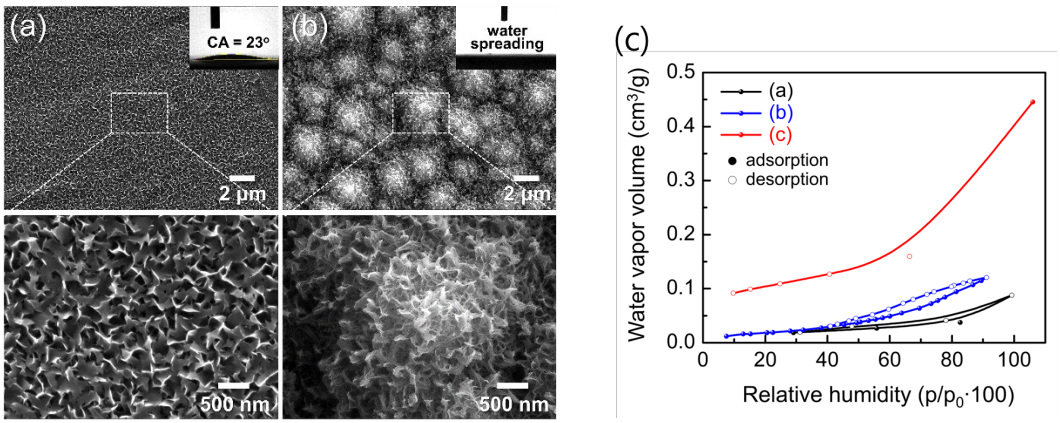

Figure 15. Low- and high-magnification SEM images of (a) flat Al/Si and (b) hierarchical AAO/t-Si surfaces after hot-water treatment for 10 min. Insets show WCAs. (c) Moisture adsorption/desorption isotherms of (a) as-prepared AAO/t-Si, (b) 800 °C-calcined Al_2O_3/t-Si, and (c) hot-water-treated boehmite [AlO(OH)]/t-Si surfaces.

Moisture adsorption/desorption isotherms (Figure 15c) further support this conclusion. All samples were pre-heated at 300 °C for 24 h under vacuum to remove physisorbed water before measurement. As RH increased, water vapor uptake proceeded through successive stages: hydroxylation, monolayer adsorption, multilayer formation, and finally capillary condensation[51, 53, 57, 90]. Hydration-to-condensation transitions near 30–40% RH confirmed the presence of nanopores on both porous surfaces. The γ-Al_2O_3/t-Si surface showed slightly higher uptake than amorphous AAO/t-Si, likely reflecting its intrinsic porosity.

Notably, the AlO(OH)/t-Si exhibited a water vapor capacity of 11.51 cm^3/g at 30% RH—five to six times higher than amorphous (1.87 cm^3/g) or γ-phase (2.27 cm^3/g) Al_2O_3/t-Si. This exceptionally

 doi:10.20944/preprints202509.1977.v1

high adsorption is attributed to both increased surface area and the high density of hydroxyl groups. However, some chemisorbed water may not have been fully removed during pre-treatment; previous studies report that annealing above 700 °C is needed to eliminate surface hydroxyls from alumina[49]. Thus, optimizing pre-treatment to remove residual –OH groups while remaining compatible with device processing could further enhance the apparent gettering capacity of these super-hydrophilic surfaces.

These results highlight that hierarchical structuring amplifies the intrinsic hydrophilicity of Al-based oxides, and that surface chemistry—particularly hydroxyl group density—plays a decisive role in enabling super-hydrophilic wetting and enhanced moisture adsorption.

3.5. Hydrophobic Surface Modification of Hierarchical Al_2O_3/Si via PFOTS Treatment

To examine the effect of surface energy modulation on wetting behavior, the hierarchical Al-based oxide surfaces were further functionalized with (1H,1H,2H,2H-perfluorooctyl)trichlorosilane (PFOTS), a fluorinated silane known to form low-surface-energy coatings. As shown in Figure 16, all PFOTS-treated samples exhibited markedly increased WCAs compared to their as-prepared states, indicating successful conversion to hydrophobic surfaces. The smooth α-Al_2O_3/Si reference (Figure 16a) showed an average WCA of 95°, consistent with previously reported values (~80°)[74].

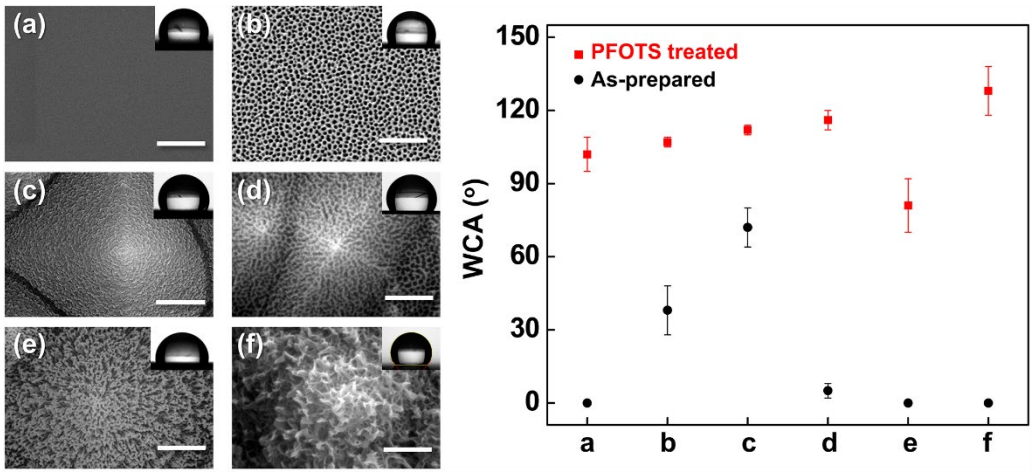

Figure 16. (Left) SEM images of (a) smooth α-Al_2O_3/Si, (b) porous AAO/Si, (c) AAO/t-Si, (d) porous AAO/t-Si, (e) wire-like Al_2O_3/t-Si, and (f) boehmite [AlO(OH)]/t-Si; (Right) WCAs measured on each surface before (black circles) and after PFOTS treatment (red squares).

Hierarchical surfaces with micro/nano dual roughness (Figure 16b–d) exhibited WCAs of 100–110° after PFOTS treatment, significantly higher than their hydrophilic as-prepared states. This enhancement is attributed to air entrapment between the surface asperities, which reduces the liquid–solid contact area in accordance with the Cassie–Baxter model[77, 78]. In contrast, collapsed porous structures (Figure 16e) showed diminished hydrophobic recovery despite PFOTS treatment, likely because the dead-end geometry prevents stable air entrapment and fails to support the Cassie–Baxter state.

Interestingly, the edge-curved nanosheet morphology of the AlO(OH)/t-Si surface (Figure 16f) exhibited both high hydrophilicity before treatment and pronounced hydrophobicity after PFOTS modification. The nanosheets act as discrete pillars supporting the droplet, resembling hierarchical mushroom-like architectures reported to enable wet self-cleaning behavior[91]. These results demonstrate that the final wettability is governed by the interplay between surface roughness hierarchy and surface free energy, and that PFOTS treatment can switch super-hydrophilic hierarchical structures to hydrophobic states when their geometry supports stable air entrapment.

 doi:10.20944/preprints202509.1977.v1

5. Conclusions

This work establishes a versatile strategy to engineer hierarchical Al_2O_3 architectures on t-Si by integrating nanoporous AAO and boehmite [AlO(OH)] layers through controlled anodization and post-treatment. Pore-widening increased the porosity of AAO (22–49%) and boosted water vapor uptake at 20% RH from 2.66 to 7.30 $cm^3\ g^{-1}$, primarily by exposing additional adsorption sites such as incorporated anionic species (O^-, O^{2-}, oxalate). Complementary thermal annealing converted amorphous AAO into γ- and α- Al_2O_3, while hot-water treatment generated hierarchical AlO(OH) nanosheets enriched with hydroxyl groups. Both approaches yielded near-zero water contact angles and rapid water spreading driven by capillary wicking and imbibition effects. Furthermore, surface fluorination with PFOTS enabled a reversible transition from super-hydrophilic to hydrophobic states via the Cassie–Baxter wetting regime.

Collectively, these findings demonstrate that hierarchical AAO/Si and AlO(OH)/Si interfaces combine high moisture gettering capacity with tunable water affinity, offering dual functionality for hermetically sealed MEMS packaging and responsive humidity sensing. This study provides a platform approach to exploit hierarchical Al_2O_3 architectures as multifunctional water-affine interfaces for next-generation MEMS-based environmental control and sensing systems.

Author Contributions: Conceptualization, H.-R.L. and Y.-H.C.; methodology, H.-R.L., T.W.Y., and N.S.A.E.; validation, H.-R.L., T.W.Y., and N.S.A.E.; formal analysis, H.-R.L., and T.W.Y.; investigation, H.-R.L., T.W.Y., and N.S.A.E.; resources, Y.-H.C.; data curation, H.-R.L.; writing—original draft preparation, H.-R.L., T.W.Y., D.K. and C.Y.H.; writing—review and editing, H.-R.L. and Y.-H.C.; visualization, H.-R.L. and N.S.A.E.; supervision, Y.-H.C.; project administration, Y.-H.C.; funding acquisition, H.-R.L. and Y.-H.C. All authors have read and agreed to the published version of the manuscript.

Funding: This work was supported by the Pukyong National University Research Fund (202126860001) and by the Global Semiconductor Advanced Fab Utilization Project through the National NanoFab Center (NNFC, RS-2024-00440903), funded by the Ministry of Science and ICT, Republic of Korea.

Institutional Review Board Statement: Not Applicable

Informed Consent Statement: Not Applicable

Data Availability Statement: The data presented in this study are available on reasonable request from the corresponding author.

Conflicts of Interest: The authors declare no conflicts of interest.

References

1. Anagnostou, D.E.; Chryssomallis, M.T.; Braaten, B.D.; Ebel, J.L.; Sepúlveda, N. Reconfigurable UWB antenna with RF-MEMS for on-demand WLAN rejection. *IEEE Trans. Antennas Propag.* 2014, 62, 602–608.
2. Chakraborty, A.; Gupta, B.; Sarkar, B.K. Design, fabrication and characterization of miniature RF MEMS switched capacitor based phase shifter. *Microelectron. J.* 2014, 45, 1093–1102.
3. Solgaard, O.; Godil, A.A.; Howe, R.T.; Lee, L.P.; Peter, Y.-A.; Zappe, H. Optical MEMS: From micromirrors to complex systems. *J. Microelectromech. Syst.* 2014, 23, 517–538.
4. Huang, Y.; Vasan, A.S.S.; Doraiswami, R.; Osterman, M.; Pecht, M. MEMS reliability review. *IEEE Trans. Device Mater. Reliab.* 2012, 12, 482–493.
5. Moraja, M.; Amiotti, M.; Kullberg, R.C. Hermetic sealing challenges for MEMS packages. *IEEE Trans. Adv. Packag.* 2002, 25, 260–267.
6. Previti, M.; Gilleo, K. Moisture ingress and getter solutions. In *Proceedings of the International Symposium on Advanced Packaging Materials Processes, Properties and Interfaces (IEEE Cat. No.01TH8562)*; IEEE: Piscataway, NJ, USA, 2001; pp. 201–206.
7. Komvopoulos, K. Surface engineering and microtribology for microelectromechanical systems. *Wear* 1996, 200, 305–327.

 doi:10.20944/preprints202509.1977.v1

8. Miller, W.M. MEMS reliability and testing. In *Proceedings of the 1999 MEMS Reliability Conference*, Chicago, IL, USA, 23–24 October 1999.
9. Srivastava, N.C.; Eames, I.W. A review of adsorbents and adsorbates in solid–vapour adsorption heat pump systems. Appl. *Therm. Eng.* 1998, 18, 707–714.
10. Ramesham, R.; Kullberg, R.C. Review of vacuum packaging and maintenance of MEMS and the use of getters therein. J. Micro/Nanolithogr. *MEMS MOEMS* 2009, 8, 031307.
11. Wu, C.-S.; Liao, J.-Y.; Fang, S.-Y.; Chiang, A.S. Flexible and transparent moisture getter film containing zeolite. *Adsorption* 2010, 16, 69–74.
12. Chuntonov, K.; Setina, J. Reactive getters for MEMS applications. *Vacuum* 2016, *123*, 42–48.
13. Busca, G. The surface of transitional aluminas: A critical review. *Catal. Today* 2014, 226, 2–13.
14. Loeb, G.I.; Schrader, M.E. *Modern Approaches to Wettability: Theory and Applications*; Springer: Berlin/Heidelberg, Germany, 2013.
15. Tavakoli, A.H.; Browning, N.D.; Arslan, I.; Gates, B.C.; Dixon, D.A.; Glezakou, V.-A. Amorphous alumina nanoparticles: Structure, surface energy, and thermodynamic phase stability. *J. Phys. Chem. C* 2013, 117, 17123–17130.
16. McHale, J.; Navrotsky, A.; Perrotta, A. Effects of increased surface area and chemisorbed H_2O on the relative stability of nanocrystalline γ-Al_2O_3 and α-Al_2O_3. *J. Phys. Chem. B* 1997, 101, 603–613.
17. Hass, K.C.; Schneider, W.F.; Curioni, A.; Andreoni, W. The chemistry of water on alumina surfaces: Reaction dynamics from first principles. *Science* 1998, 282, 265–268.
18. Wippermann, S.; Schmidt, W.G.; Thissen, P.; Grundmeier, G. Dissociative and molecular adsorption of water on α-Al_2O_3 (0001). *Phys. Status Solidi C* 2010, 7, 137–140.
19. Trueba, M.; Trasatti, S.P. γ-Alumina as a support for catalysts: A review of fundamental aspects. *Eur. J. Inorg. Chem.* 2005, 3393–3403.
20. Wang, S.; Liu, K.; Yao, X.; Jiang, L. Bioinspired surfaces with superwettability: New insight on theory, design, and applications. *Chem. Rev.* 2015, 115, 8230–8293.
21. Drelich, J.; Chibowski, E.; Meng, D.D.; Terpilowski, K. Hydrophilic and superhydrophilic surfaces and materials. *Soft Matter* 2011, 7, 9804–9828.
22. Guo, Z.; Zhou, F.; Hao, J.; Liu, W. Stable biomimetic super-hydrophobic engineering materials. *J. Am. Chem. Soc.* 2005, 127, 15670–15671.
23. Fu, X.; He, X. Fabrication of super-hydrophobic surfaces on aluminum alloy substrates. *Appl. Surf. Sci.* 2008, 255, 1776–1781.
24. Sarkar, D.K.; Farzaneh, M. Superhydrophobic Coatings with Reduced Ice Adhesion. *J. Adhes. Sci. Technol.* 2009, 23, 1215–1237.
25. Saleema, N.; Farzaneh, M.; Paynter, R.W.; Sarkar, D.K. Prevention of Ice Accretion on Aluminum Surfaces by Enhancing Their Hydrophobic Properties. *J. Adhes. Sci. Technol.* 2011, 25, 27–40.
26. Saleema, N.; Sarkar, D.; Gallant, D.; Paynter, R.; Chen, X.-G. Chemical nature of superhydrophobic aluminum alloy surfaces produced via a one-step process using fluoroalkyl-silane in a base medium. *ACS Appl. Mater. Interfaces* 2011, 3, 4775–4781.
27. Ye, J.; Yin, Q.; Zhou, Y. Superhydrophilicity of anodic aluminum oxide films: From "honeycomb" to "bird's nest". *Thin Solid Films* 2009, 517, 6012–6015.
28. Kim, Y.; et al. Robust Superhydrophilic/Hydrophobic Surface Based on Self-Aggregated Al_2O_3 Nanowires by Single-Step Anodization and Self-Assembly Method. *ACS Appl. Mater. Interfaces* 2012, 4, 5074–5078.
29. Buijnsters, J.G.; Zhong, R.; Tsyntsaru, N.; Celis, J.-P. Surface wettability of macroporous anodized aluminum oxide. *ACS Appl. Mater. Interfaces* 2013, 5, 3224–3233.
30. Kiyoharu, T.; Noriko, K.; Tsutomu, M. Super-Water-Repellent Al_2O_3 Coating Films with High Transparency. *J. Am. Ceram. Soc.* 1997, 80, 1040–1042.
31. Kiyoharu, T.; Noriko, K.; Tsutomu, M. Formation Process of Super-Water-Repellent Al_2O_3 Coating Films with High Transparency by the Sol–Gel Method. *J. Am. Ceram. Soc.* 1997, 80, 3213–3216.
32. Jafari, R.; Farzaneh, M. Fabrication of superhydrophobic nanostructured surface on aluminum alloy. *Appl. Phys. A* 2011, 102, 195–199.

33. Cho, H.; Kim, D.; Lee, C.; Hwang, W. A simple fabrication method for mechanically robust superhydrophobic surface by hierarchical aluminum hydroxide structures. *Curr. Appl. Phys.* 2013, 13, 762–767.
34. Feng, L.; Che, Y.; Liu, Y.; Qiang, X.; Wang, Y. Fabrication of superhydrophobic aluminium alloy surface with excellent corrosion resistance by a facile and environment-friendly method. *Appl. Surf. Sci.* 2013, 283, 367–374.
35. Feng, L.; Zhang, H.; Wang, Z.; Liu, Y. Superhydrophobic aluminum alloy surface: Fabrication, structure, and corrosion resistance. *Colloids Surf. A Physicochem. Eng. Asp.* 2014, 441, 319–325.
36. Zuo, Z.; et al. Fabrication and Anti-icing Property of Coral-like Superhydrophobic Aluminum Surface. *Appl. Surf. Sci.* 2015.
37. Kim, J.; Jun, S.; Lee, J.; Godinez, J.; You, S.M. Effect of Surface Roughness on Pool Boiling Heat Transfer of Water on a Superhydrophilic Aluminum Surface. *J. Heat Transf.* 2017, 139, 101501.
38. Sharma, C.S.; Combe, J.; Giger, M.; Emmerich, T.; Poulikakos, D. Growth Rates and Spontaneous Navigation of Condensate Droplets Through Randomly Structured Textures. *ACS Nano* 2017, 11, 1673–1682.
39. Parin, R.; et al. Nano-structured aluminum surfaces for dropwise condensation. *Surf. Coat. Technol.* 2018, 348, 1–12.
40. Ngo, C.-V.; Chun, D.-M. Control of laser-ablated aluminum surface wettability to superhydrophobic or superhydrophilic through simple heat treatment or water boiling post-processing. *Appl. Surf. Sci.* 2018, 435, 974–982.
41. Zubel, I.; Kramkowska, M. The effect of isopropyl alcohol on etching rate and roughness of (100) Si surface etched in KOH and TMAH solutions. *Sens. Actuators A Phys.* 2001, 93, 138–147.
42. Papet, P.; Nichiporuk, O.; Kaminski, A.; Rozier, Y.; Kraiem, J.; Lelievre, J.F.; Chaumartin, A.; Fave, A.; Lemiti, M. Pyramidal texturing of silicon solar cell with TMAH chemical anisotropic etching. *Sol. Energy Mater. Sol. Cells* 2006, 90, 2319–2328.
43. Diggle, J. W., Downie, T. C. & Goulding, C. W. Anodic oxide films on aluminum. Chemical Reviews 69, 365-405, doi:10.1021/cr60259a005 (1969).
44. Sousa, C. T. et al. Nanoporous alumina as templates for multifunctional applications. Applied Physics Reviews 1, -, doi:doi:http://dx.doi.org/10.1063/1.4893546 (2014).
45. Yang, Y. et al. Anodic alumina template on Au/Si substrate and preparation of CdS nanowires. Solid State Commun. 123, 279-282 (2002).
46. Masuda, H. & Fukuda, K. Ordered metal nanohole arrays made by a two-step replication of honeycomb structures of anodic alumina. science 268, 1466-1468 (1995).
47. Nielsch, K., Choi, J., Schwirn, K., Wehrspohn, R. B. & Gösele, U. Self-ordering regimes of porous alumina: the 10 porosity rule. Nano Lett. 2, 677-680 (2002).
48. Mata-Zamora, M. & Saniger, J. Thermal evolution of porous anodic aluminas: a comparative study. Revista mexicana de física 51, 502-509 (2005).
49. Mardilovich, P. P., Govyadinov, A. N., Mukhurov, N. I., Rzhevskii, A. M. & Paterson, R. New and modified anodic alumina membranes Part I. Thermotreatment of anodic alumina membranes. Journal of Membrane Science 98, 131-142, doi:http://dx.doi.org/10.1016/0376-7388(94)00184-Z (1995).
50. Yang, S. G. et al. Stability of anodic aluminum oxide membranes with nanopores. Physics Letters A 318, 440-444, doi:http://dx.doi.org/10.1016/j.physleta.2003.09.051 (2003).
51. Al-Abadleh, H. A. & Grassian, V. FT-IR study of water adsorption on aluminum oxide surfaces. Langmuir 19, 341-347 (2003).
52. Loeb, G. I. & Schrader, M. E. Modern approaches to wettability: theory and applications. (Springer Science & Business Media, 2013).
53. Fubini, B., Della Gatta, G. & Venturello, G. Energetics of adsorption in the alumina—water system microcalorimetric study on the influence of adsorption temperature on surface processes. Journal of Colloid and Interface Science 64, 470-479 (1978).
54. Hass, K. C., Schneider, W. F., Curioni, A. & Andreoni, W. The chemistry of water on alumina surfaces: Reaction dynamics from first principles. science 282, 265-268 (1998).

55. Verdaguer, A., Sacha, G. M., Bluhm, H. & Salmeron, M. Molecular Structure of Water at Interfaces: Wetting at the Nanometer Scale. Chemical Reviews 106, 1478-1510, doi:10.1021/cr040376l (2006).
56. Thomas, A. C. & Richardson, H. H. Growth of Thin Film Water on α-Al2O3 (0001): An FTIR Study. The Journal of Physical Chemistry C 112, 20033-20037 (2008).
57. Choi, J. et al. Perfect two-dimensional porous alumina photonic crystals with duplex oxide layers. Journal of Applied Physics 94, 4757-4762, doi:10.1063/1.1609033 (2003).
58. Lujun, Y., Maojun, Z., Haibin, L., Li, M. & Wenzhong, S. High-performance humidity sensors based on high-field anodized porous alumina films. Nanotechnology 22, 379501 (2011).
59. Ono, S., Ichinose, H. & Masuko, N. The high resolution observation of porous anodic films formed on aluminum in phosphoric acid solution. Corrosion Science 33, 841-850, doi:https://doi.org/10.1016/0010-938X(92)90048-8 (1992).
60. Xiong, G. et al. Effect of Atomic Layer Deposition Coatings on the Surface Structure of Anodic Aluminum Oxide Membranes. The Journal of Physical Chemistry B 109, 14059-14063, doi:10.1021/jp0503415 (2005).
61. Eng, P. J. et al. Structure of the Hydrated α-Al₂O₃ (0001) Surface. Science 288, 1029 (2000).
62. Liu, X. & Truitt, R. E. DRFT-IR Studies of the Surface of γ-Alumina. Journal of the American Chemical Society 119, 9856-9860, doi:10.1021/ja971214s (1997).
63. Chatterjee, M., Enkhtuvshin, D., Siladitya, B. & Ganguli, D. Hollow Alumina Microspheres From Boehmite Sols. J Mater Sci 33, 4937-4942, doi:10.1023/a:1004430218980 (1998).
64. Young, L. Anodic oxide films. (London; New York: Academic Press, 1961).
65. Emmer, I., Hajek, Z. & Řepa, P. Surface adsorption of water vapor on hydrated layers of Al2O3. Surface Science 162, 303-309 (1985).
66. Park, B. K., Lee, Y. S. & Koo, K. K. Preparation of highly porous aluminum hydroxide gels by hydrolysis of an alumi-num sulfate and mineralizer. Journal of Ceramic Processing Research 11, 64-68 (2010).
67. Monica, T. & P., T. S. γ-Alumina as a Support for Catalysts: A Review of Fundamental Aspects. European Journal of Inorganic Chemistry 2005, 3393-3403, doi:doi:10.1002/ejic.200500348 (2005).
68. Wenzel, R. N. RESISTANCE OF SOLID SURFACES TO WETTING BY WATER. Industrial & Engineering Chemistry 28, 988-994, doi:10.1021/ie50320a024 (1936).
69. Wenzel, R. N. Surface Roughness and Contact Angle. The Journal of Physical and Colloid Chemistry 53, 1466-1467, doi:10.1021/j150474a015 (1949).
70. Leem, J. W., Dudem, B. & Yu, J. S. Biomimetic nano/micro double-textured silicon with outstanding antireflective and super-hydrophilic surfaces for high optical performance. RSC Advances 7, 33757-33763, doi:10.1039/C7RA06444F (2017).
71. Bico, J., Tordeux, C. & Quéré, D. Rough wetting. EPL (Europhysics Letters) 55, 214 (2001).
72. Cassie, A. B. D. Contact angles. Discussions of the Faraday Society 3, 11-16, doi:10.1039/DF9480300011 (1948).
73. Cassie, A. B. D. & Baxter, S. Wettability of porous surfaces. Transactions of the Faraday Society 40, 546-551, doi:10.1039/TF9444000546 (1944).
74. Redon, R. et al. Contact angle studies on anodic porous alumina. Journal of colloid and interface science 287, 664-670 (2005).
75. Chen, Z. & Lu, C. Humidity sensors: a review of materials and mechanisms. Sensor letters 3, 274-295 (2005).
76. Henderson, M. A. The interaction of water with solid surfaces: fundamental aspects revisited. Surface Science Reports 46, 1-308 (2002).
77. Zhang, D., Wang, Y. & Gan, Y. Characterization of critically cleaned sapphire single-crystal substrates by atomic force microscopy, XPS and contact angle measurements. Applied Surface Science 274, 405-417, doi:https://doi.org/10.1016/j.apsusc.2012.12.143 (2013).
78. Spooner, R. C. Water Sealing of Detached Aluminium Oxide Anodic Film. Nature 178, 1113-1114 (1956).
79. Hart, R. A study of boehmite formation on aluminium surfaces by electron diffraction. Trans. Faraday Soc. 50, 269-273 (1954).

 doi:10.20944/preprints202509.1977.v1

80. Seo, Y. I., Lee, Y. J., Kim, D.-G., Lee, K. H. & Kim, Y. D. Mechanism of aluminum hydroxide layer formation by surface modification of aluminum. Applied Surface Science 256, 4434-4437, doi:http://dx.doi.org/10.1016/j.apsusc.2010.01.011 (2010).
81. Hozumi, A., Kim, B. & McCarthy, T. J. Hydrophobicity of Perfluoroalkyl Isocyanate Monolayers on Oxidized Aluminum Surfaces. Langmuir 25, 6834-6840, doi:10.1021/la804127z (2009).
82. Tadanaga, K., Katata, N. & Minami, T. Formation Process of Super-Water-Repellent Al2O3 Coating Films with High Transparency by the Sol–Gel Method. Journal of the American Ceramic Society 80, 3213-3216 (1997).
83. Łodziana, Z., Topsøe, N.-Y. & Nørskov, J. K. A negative surface energy for alumina. Nature materials 3, 289 (2004).
84. Kim, S., Cheung, E. & Sitti, M. Wet Self-Cleaning of Biologically Inspired Elastomer Mushroom Shaped Microfibrillar Adhesives. Langmuir 25, 7196-7199, doi:10.1021/la900732h (2009).